Fast numerical estimation of residual stresses induced by laser shock peening

L. Lapostolle *, L. Morin, K. Derrien, L. Berthe, O. Castelnau

PIMM, Arts et Metiers Institute of Technology, CNRS, Cnam, HESAM University, 151 boulevard de l'Hopital, 75013 Paris, France

A B S T R A C T

The aim of this paper is to develop a model allowing a fast first approximate estimation of the elastic–plastic stress wave propagation caused by a laser impact and the resulting residual stress field. We start by modeling the stress wave propagation, adopting a 1D uniaxial modeling, reducing the behavior of the specimen to the axis of the laser impact, excluding any edge effects caused by the edges of the laser spot. The plastic strain field resulting from this propagation can in turn be used to compute the residual stresses, by making use of an analytic modeling in the case of an infinite planar plate. The accuracy of the 1D model is assessed by comparing it to finite elements simulations, acting as a reference solution, for several materials and laser spot diameters. The results show that the stress wave propagation from the 1D model is close to identical to the reference solution. The residual plastic and stress fields from the finite elements model present a uniaxial distribution on a large portion of the laser spot, except for the very edge and spot center. The comparison between the 1D model and the reference solution shows a good match, indicating that the 1D model can be used for a fast approximation the mechanical fields created by a laser impact for laser spot diameters larger than 2 mm.

1. Introduction

The Laser Shock Peening (LSP) process is a surface treatment aiming to induce compressive residual stresses in a material. A high energy laser beam (> GW/cm^2) is used to impact the surface of the material, creating a high pressure plasma. The expansion of this plasma transmits energy to the material in the form of a pressure wave, with an amplitude of a few GPa and a time duration of a few dozens of nanoseconds, generating plastic strains on its path (Fig. 1). The pressure profile of the plasma was modeled in several works (Fabbro et al., 1990; Scius-Bertrand et al., 2021; Rondepierre et al., 2021). The relaxation of the material in turn creates compressive residual stresses, which have been shown to increase the fatigue resistance of the specimen (Ding and Ye, 2006a; Peyre et al., 1998, 1996). To increase the amount of energy transmitted from the plasma into the material, water is used as confinement in experimental setups (Fox, 1974). In addition, the specimen is generally covered by a protective coating to avoid thermal effects (which could lead to tensile stresses at the surface). The main applications of LSP currently reside in the aeronautics and energy industries (Montross et al., 2002; Clauer, 2019).

The modeling and simulation of LSP started decades ago with the seminal works of Ballard (1991) (see also Ballard et al., 1991; Heuzé, 2017) and Braisted (1999) using Finite Element (FE) models. LSP simulations consider the propagation of a stress wave in an elastic–plastic material induced by a dynamic pressure impulse. The impacted specimen is modeled by an isotropic homogeneous material in most cases. Given the range of pressure of LSP, the elastic behavior can incorporate a hydrodynamic component in the form of an Equation of State (EOS) (Peyre et al., 2012, 2003). The plastic behavior is generally modeled by the Johnson–Cook model (Johnson and Cook, 1983), which accounts for the strain-rate dependency of the behavior. The simulations thus allow the study of various model parameters, such as the laser spot size, and the overlapping of several laser shots (Brockman et al., 2012; Song, 2010; Hfaiedh et al., 2015; Adu-Gyamfi et al., 2018). The behaviors of materials under laser impact loading were successfully reproduced in several 3D FE simulations when compared to experimental results, see for example (Peyre et al., 2007; Seddik et al., 2022).

Once the heterogeneous plastic strain field has been correctly computed in the material by solving the stress wave propagation problem, it can be used to determine the resulting residual stresses remaining in the material after the relaxation, using various methods. The residual stresses were initially linked analytically to eigenstrains (such as plastic strains), which do not generate stress on their own but by their heterogeneous distribution in the material, leading to strain incompatibilities, to which the specimen reacts by generating elastic strains (Johns, 1965; Korsunsky, 2005; Gelineau, 2018; Cochennec, 2009; Ahdad and Desvignes, 1996). Similarly, the Almen strip deflection method can be

used the compute the residual stresses in a thin sample by combining analytical solution and experimental measurements (Glaser et al., 2022; Miao et al., 2010). Other analytical solutions exist. Taddia and Troiani (2015) use a formula for the surface distribution of residual stresses introduced by Tada and Paris (1983). However this concerns only the surface residual stresses, while we are interested by the in-depth residual stresses, and the function used is artificially constructed and does not stem from physical models. Because such analytical solutions are valid only for specific specimen geometries, numerical simulations offer a wider array of possibilities. The recent work of Cai (2022) presents a methodology where only the final equilibrium is simulated, allowing the reconstruction of the 3D residual stress field induced by a laser impact from particular experimental data points. Some literature works (Peyre et al., 2012, 2007) use a single dynamic explicit numerical algorithm for both the stress wave propagation and the relaxation, with a simulation duration several order of magnitudes longer than the pulse duration (a few dozens of milliseconds for a single impact lasting a few dozens of nanoseconds), leaving enough time for the kinetic energy to dissipate. On the other hand, several works (Seddik et al., 2022; Achintha and Nowell, 2011; Ocaña et al., 2004; Achintha et al., 2013) use an explicit analysis for the stress wave propagation, which generates a plastic strain field, followed by an implicit relaxation step. Brockman et al. (2012) uses a hybrid methodology, using explicit and implicit procedures for the several relaxation steps necessary in their multiple shots simulations. Because of the small time increment necessary for explicit procedures to yield stable results, they are often inappropriate for long simulation times, such as the ones required for several impacts simulations. Overall, obtaining the residual stresses generated by a LSP using a FE approach is computationally demanding, and requires specific modeling techniques.

The aim of this paper is to provide a tool to give a fast first approximation of the mechanical fields during the impact and of the residual stresses induced by LSP. To do so, we develop a 1D modeling composed of the following steps:

(1) An explicit numerical uniaxial resolution of the elasto-plastic stress wave propagation. This step is necessary to compute the plastic strain fields induced by the stress wave.
(2) An analytic computation of the residual stresses based on the plastic strain field generated in the previous step, using eigenstrain-based methods.

To assess this approximate modeling, we compare it to a reference 3D FE axisymmetric model. Though this 1D approach cannot capture some features of the axisymmetric fields, we show that a large part of the impacted zone can be approximated by a uniaxial field. We give numerical examples for various materials having a strain-rate dependent behavior. The proposed approximation can be useful to provide a first insight into the residual stresses induced on a given material, or as a calibration tool to determine an initial estimation of the material parameters. The numerical tool, which is made available, can reach results in close agreement with the FE models, but orders of magnitude faster, and is simple to use.

The paper is organized as follows. In Section 2 we present the mechanical framework, derive the stress wave propagation equations for an elastic–plastic behavior with a strain-rate dependent behavior, and detail the numerical method used for the simulations. The obtained plastic strain field is then used for the analytic residual stress computations based on eigenstrains methods. Then in Section 3, we perform numerical tests on various materials, to assess the propagation step of our model by investigating the backface velocity profiles and comparing it to a FE reference solution. Finally in Section 4 we apply the same methodology to assess the distribution of the residual fields induced by the stress wave propagation, by comparison to a reference FE solution. The numerical tool used here, named EVEREST, is made available under LGPL license (Lapostolle, 2022).

2. A 1D model for the stress wave propagation and the resulting residual stress field

The aim of this section is to present a simple 1D model for the residual stresses caused by the propagation of an elasto-plastic stress wave induced by a laser shock. Such a model cannot replace more complex and accurate 3D models, but can be used as an initial modeling of the problem.

2.1. Mechanical behavior

In this work we consider an isotropic homogeneous material with an elasto-plastic behavior, which is described by the following equations (in the absence of body force):

$$\begin{cases} \operatorname{div}(\boldsymbol{\sigma}) = \rho \dfrac{\partial^2 \boldsymbol{u}}{\partial t^2} & \text{Dynamic equilibrium} \\ \boldsymbol{\sigma} = \mathbb{C} : \boldsymbol{\varepsilon}_e = \mathbb{C} : (\boldsymbol{\varepsilon} - \boldsymbol{\varepsilon}_p) & \text{Hooke's Law} \\ \boldsymbol{\varepsilon}(\boldsymbol{u}) = \dfrac{1}{2}\left(\nabla \boldsymbol{u} + \nabla^T \boldsymbol{u}\right) & \text{Strain–displacement relation} \\ g = \sigma_{\text{eq}} - R \leq 0 & \text{Plasticity criterion} \\ \begin{cases} \dot{\boldsymbol{\varepsilon}}_p = \dot{\lambda} \dfrac{\partial g}{\partial \boldsymbol{\sigma}} \\ \dot{\lambda} \geq 0 \\ \dot{\lambda} g = 0, \end{cases} & \text{Flow rule and consistency conditions} \end{cases} \tag{1}$$

where $\boldsymbol{\sigma}$ is the stress tensor, $\boldsymbol{\varepsilon}$ the total strain tensor, $\boldsymbol{\varepsilon}_e$ the elastic strain tensor, $\boldsymbol{\varepsilon}_p$ the plastic strain tensor and $\boldsymbol{u}$ the displacement field. In the flow rule and consistency conditions, λ is the (standard) plastic multiplier, whose time derivative is either zero when $g < 0$ (purely elastic response), or positive when $g = 0$ (plastic strains occur), as enforced by the condition $\dot{\lambda} g = 0$. The quantity ρ is the density of the material, and $\mathbb{C}$ is the fourth-order stiffness tensor which is given by

$$\mathbb{C} = 3\kappa \mathbb{J} + 2\mu \mathbb{K}, \tag{2}$$

where κ and μ are the bulk and shear moduli respectively. $\mathbb{C}$ is assumed to be isotropic, although the developments can be easily extended to anisotropic materials. The fourth-order tensors $\mathbb{J}$ and $\mathbb{K}$ are given by

$$\mathbb{J} = \frac{1}{3} \boldsymbol{I} \otimes \boldsymbol{I} \quad \text{and} \quad \mathbb{K} = \mathbb{I} - \mathbb{J}, \tag{3}$$

$\boldsymbol{I}$ being the second-order identity tensor, and $\mathbb{I}$ the fourth-order identity tensor. In the yield criterion, R is the yield stress and σ_{eq} is the von Mises equivalent stress which reads

$$\sigma_{\text{eq}} = \sqrt{\frac{3}{2} \boldsymbol{\sigma}_d : \boldsymbol{\sigma}_d}, \quad \boldsymbol{\sigma}_d = \boldsymbol{\sigma} - \frac{1}{3} \operatorname{Tr}(\boldsymbol{\sigma}) \boldsymbol{I}, \tag{4}$$

where $\boldsymbol{\sigma}_d$ is the deviator of the stress tensor. $\operatorname{Tr}(\cdot)$ is the trace operator.

LSP is characterized by very high strain rates ($\sim 10^6$ s^{-1}). Accounting for the strain rate dependency of the material's behavior is essential. Hence, an adapted plasticity model should be employed. Furthermore, for our applications, we will neglect the variations of temperature, by considering the experimental configuration including a protective coating (Hu and Grandhi, 2012). This coating was shown to absorb thermal effects (Gill et al., 2015; Rubio-González et al., 2006). We thus neglect any thermal strains, or changes in the material properties caused by the temperature rise. The model commonly used in the literature (Julan, 2014; Julan et al., 2014; Amarchinta et al., 2009; Chaieb, 2004; Peyre et al., 2012, 2007) is the Johnson–Cook plasticity model (Johnson and Cook, 1983), for which the yield stress R is given by (without the influence of the temperature):

$$R(p, \dot{p}) = (A + B p^n) \left(1 + C \ln\left(\frac{\dot{p}}{\dot{\varepsilon}_0}\right)\right), \tag{5}$$

where $\dot{p}$ is the (von Mises) equivalent strain rate and p is the accumulated plastic strain defined by

$$\dot{p} = \sqrt{\frac{2}{3} \dot{\boldsymbol{\varepsilon}}_p : \dot{\boldsymbol{\varepsilon}}_p}, \quad p = \int_0^t \dot{p}(\tau) \mathrm{d}\tau. \tag{6}$$

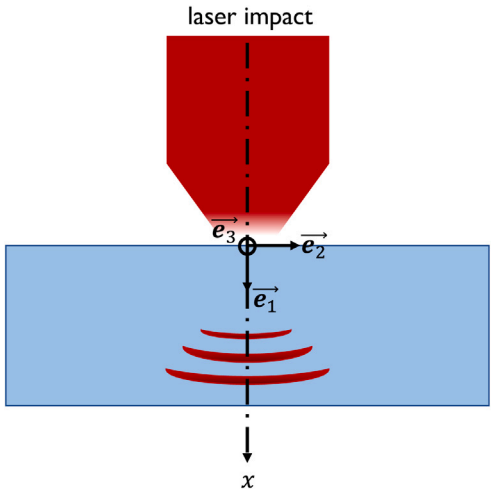

Fig. 1. Illustration of the LSP process.

For this model, it can be shown that $\dot{\lambda} = \dot{p}$. In Eq. (5), A, B, C, n and $\dot{\varepsilon}_0$ are parameters to be determined. For our applications, we will not consider any kinematic hardening. Kinematic hardening is needed when the load has a cyclic nature, as in the case of repeated impacts, a situation that we will not consider in this paper. Such developments are left for future works.

It should be noted that the elastic behavior of the material is described by Hooke's law, instead of an Equation of State (EOS), as it is usually done for LSP simulations (Peyre et al., 2012, 2007; Seddik et al., 2022). An EOS is generally necessary to describe the hydrodynamic behavior of a material when subjected to a shock loading with high pressure and strain rate. Nonetheless, in the context of this work (i.e. the determination of the residual stress field), EOS can be neglected because, as shown by Chaieb (2004), it has little effect on the residual stress field generated by the stress wave propagation. Moreover, according to Ballard (1991) (see also Ballard et al., 1991; Heuzé, 2017), the hydrodynamic behavior of a material can be neglected if the applied pressure is under 0.1κ, which is of the order of a dozen of GPa for our applications. We will check that this condition is verified in our applications.

Eqs. (1) to (6) can be used to describe the propagation of an elasto-plastic stress wave. This problem can be separated into two sequential calculation steps, the first one computing the propagation of an elastic wave, the second applying a plastic correction when needed.

2.2. Stress wave propagation step

2.2.1. Stress wave equation for an axisymmetric configuration

We derive here the expression of the equations governing the stress wave propagation, following the methodology of Ballard (1991), Ballard et al. (1991) and Heuzé (2017) (see also Lapostolle et al., 2022; Ayad et al., 2022). To that aim we adopt the small displacement hypothesis, and consider a circular laser spot. The stress and strain fields which are solutions of the problem are thus axisymmetric. Thereafter, we restrict the analysis along the symmetry axis, denoted by $\boldsymbol{e}_1$ in Fig. 1. Hence the displacement and total strain field are uniaxial and read:

$$\boldsymbol{u}(x,t) = u_1(x,t)\boldsymbol{e}_1 \quad \text{and} \quad \boldsymbol{\varepsilon}(x,t) = \varepsilon_{11}(x,t)\boldsymbol{e}_1 \otimes \boldsymbol{e}_1, \tag{7}$$

with $\varepsilon_{11} = \partial u_1/\partial x$, x being the coordinate in the $\boldsymbol{e}_1$ direction. This situation is as though the laser spot were infinite in the planar directions $\boldsymbol{e}_2$ and $\boldsymbol{e}_3$. Furthermore, the (isochoric) plastic strain field is of the form

$$\boldsymbol{\varepsilon}_p(x,t) = \varepsilon_p(x,t)\left(\boldsymbol{e}_1 \otimes \boldsymbol{e}_1 - \frac{1}{2}\left(\boldsymbol{e}_2 \otimes \boldsymbol{e}_2 + \boldsymbol{e}_3 \otimes \boldsymbol{e}_3\right)\right). \tag{8}$$

Using Eqs. $(1)_1$, (7) and (8), it follows that the stress field is of the form

$$\boldsymbol{\sigma}(x,t) = \sigma_{11}(x,t)\boldsymbol{e}_1 \otimes \boldsymbol{e}_1 + \sigma_{22}(x,t)\left(\boldsymbol{e}_2 \otimes \boldsymbol{e}_2 + \boldsymbol{e}_3 \otimes \boldsymbol{e}_3\right), \tag{9}$$

with

$$\begin{cases} \sigma_{11}(x,t) = \left(\kappa + \frac{4}{3}\mu\right)\varepsilon_{11}(x,t) - 2\mu\varepsilon_p(x,t) \\ \sigma_{22}(x,t) = \left(\kappa - \frac{2}{3}\mu\right)\varepsilon_{11}(x,t) + \mu\varepsilon_p(x,t). \end{cases} \tag{10}$$

It follows, from the dynamic equilibrium and Hooke's law in Eq. (1), that the wave propagation equations reduce to

$$\begin{cases} \dfrac{\partial \sigma_{11}}{\partial x}(x,t) = \rho\dfrac{\partial v_1}{\partial t}(x,t) \\ \dfrac{\partial \sigma_{11}}{\partial t}(x,t) = \left(\kappa + \dfrac{4}{3}\mu\right)\dfrac{\partial \varepsilon_{11}}{\partial t}(x,t) - 2\mu\dfrac{\partial \varepsilon_p}{\partial t}(x,t), \end{cases} \tag{11}$$

where $v_1 = \partial u_1/\partial t$ is the material velocity in the direction of the impact. By taking advantage of the relation

$$\frac{\partial \varepsilon_{11}}{\partial t} = \frac{\partial}{\partial t}\left(\frac{\partial u_1}{\partial x}\right) = \frac{\partial}{\partial x}\left(\frac{\partial u_1}{\partial t}\right) = \frac{\partial v_1}{\partial x}, \tag{12}$$

the system in Eq. (11) thus becomes

$$\begin{cases} \dfrac{\partial \sigma_{11}}{\partial x}(x,t) = \rho\dfrac{\partial v_1}{\partial t}(x,t) \\ \dfrac{\partial \sigma_{11}}{\partial t}(x,t) = \left(\kappa + \dfrac{4}{3}\mu\right)\dfrac{\partial v_1}{\partial x}(x,t) - 2\mu\dfrac{\partial \varepsilon_p}{\partial t}(x,t). \end{cases} \tag{13}$$

System (13) is used to model the elastic–plastic stress wave propagation, which we will now detail the resolution.

2.2.2. Elastic propagation

The first step to solve the stress wave propagation system (13) is to compute the trial elastic predictor, by assuming (momentarily) that the rate of the plastic strain is null ($\partial\varepsilon_p/\partial t = 0$). In that case, Eq. (13) can be written in the following matrix form:

$$\frac{\partial \boldsymbol{U}}{\partial t} + \boldsymbol{A}\frac{\partial \boldsymbol{U}}{\partial x} = 0, \tag{14}$$

with

$$\boldsymbol{U} = \begin{pmatrix} \sigma_{11} \\ v_1 \end{pmatrix} \quad \text{and} \quad \boldsymbol{A} = \begin{pmatrix} 0 & -\left(\kappa + \frac{4}{3}\mu\right) \\ -\dfrac{1}{\rho} & 0 \end{pmatrix}. \tag{15}$$

Eq. (14) is called the advection equation, and is a hyperbolic system of partial differential equations (PDE). As such, it can be numerically solved by a large variety of dedicated explicit algorithms based on the finite-volumes approach (Leveque, 2002).

We subdivide the time and spatial domain of our problem and introduce the space and time increments Δx and Δt, and the notations $(.)_i$ and $(.)^k$ corresponding to a given spatial cell and time increment respectively. Thus $x_i = x_{i-1} + \Delta x$, $t^k = t^{k-1} + \Delta t$, and $\boldsymbol{u}\left(x_i, t^k\right) = \boldsymbol{u}_i^k$, with $1 \leq i \leq N$, N being the number of nodes. The numerical methods considered for this problem are explicit, and must respect the so-called Courant–Friedrichs–Lewy (CFL) condition:

$$\text{CFL} = c\frac{\Delta t}{\Delta x} \leq 1, \tag{16}$$

where c is the maximum compressive/tensile stress wave velocity. It is given by

$$c = \sqrt{\frac{1}{\rho}\frac{\partial \sigma_{11}}{\partial \varepsilon_{11}}}, \tag{17}$$

which reduces, in the case of an isotropic elastic medium, to

$$c = \sqrt{\left(\kappa + \frac{4}{3}\mu\right)/\rho}. \tag{18}$$

It is worth noting that in the case of an elastic–plastic evolution, the maximum value of the velocity c is achieved during the elastic propagation since the tangent modulus is lower when plastic strains are generated. Hence, the value considered in all cases for c is the

one given by Eq. (18). In practice, the CFL condition (16) is used to compute the maximum value of the time increment Δt, for a given spatial discretization (Δx), material properties (κ, μ and ρ) and CFL value.

We consider a Godunov-type algorithm (Leveque, 2002; LeVeque, 1997) which combines simplicity and accuracy as it permits to avoid spurious numerical effects as oscillations and damping (Lapostolle et al., 2022). Let us denote $\boldsymbol{U}_i^k$ the unknown vector at the time increment k and at the spatial cell i. The numerical resolution of Eq. (14) is done by computing $\boldsymbol{U}_i^{k+1}$ with

$$\boldsymbol{U}_i^{k+1} = \boldsymbol{U}_i^k - \frac{\Delta t}{\Delta x}\left(\boldsymbol{F}_{i+1/2}^k - \boldsymbol{F}_{i-1/2}^k\right). \tag{19}$$

In Eq. (19), the quantities $\boldsymbol{F}_{i+1/2}^k$ and $\boldsymbol{F}_{i-1/2}^k$ are given by

$$\boldsymbol{F}_{i+1/2}^k = \boldsymbol{A}^+\boldsymbol{U}_i^k + \boldsymbol{A}^-\boldsymbol{U}_{i+1}^k, \quad \boldsymbol{F}_{i-1/2}^k = \boldsymbol{A}^+\boldsymbol{U}_{i-1}^k + \boldsymbol{A}^-\boldsymbol{U}_i^k, \tag{20}$$

where $\boldsymbol{A}^+$ and $\boldsymbol{A}^-$ are the matrices defined by

$$\boldsymbol{A}^+ = \boldsymbol{P}\begin{pmatrix} c & 0 \\ 0 & 0 \end{pmatrix}\boldsymbol{P}^{-1} \quad \boldsymbol{A}^- = \boldsymbol{P}\begin{pmatrix} 0 & 0 \\ 0 & -c \end{pmatrix}\boldsymbol{P}^{-1}, \tag{21}$$

with $\boldsymbol{P}$ being the matrix composed of the eigenvectors of $\boldsymbol{A}$, here given by:

$$\boldsymbol{P} = \begin{pmatrix} -\sqrt{\rho\left(\kappa + \frac{4}{3}\mu\right)} & \sqrt{\rho\left(\kappa + \frac{4}{3}\mu\right)} \\ 1 & 1 \end{pmatrix}. \tag{22}$$

With this numerical method, the unknown $\boldsymbol{U}_i^{k+1}$ is obtained by linear combination of the (known) quantities $\boldsymbol{U}_{i-1}^k$, $\boldsymbol{U}_i^k$ and $\boldsymbol{U}_{i+1}^k$ at the previous time increment. To solve this problem efficiently, Eq. (19) is written as

$$\boldsymbol{X}^{k+1} = \boldsymbol{D}\boldsymbol{X}^k, \tag{23}$$

with $\boldsymbol{X}^k = \begin{pmatrix}\boldsymbol{U}_1^k & \boldsymbol{U}_2^k & \dots & \boldsymbol{U}_N^k\end{pmatrix}^T$ and $\boldsymbol{D}$ is a matrix constructed from $\boldsymbol{A}^+$ and $\boldsymbol{A}^-$. It should be noted that several improvements of the Godunov method, based on non-linear flux limiters, permit to improve the quality of the solution field in the presence of discontinuous solutions (Leveque, 2002; Heuzé, 2017). Nonetheless, since the numerical applications in the paper will only consider homogeneous material and smooth loading signals, non-linear flux limiters are not considered and Eq. (23) is used.

This elastic propagation step is used to compute at the time t^{k+1} the material velocity v_1 and the stress component σ_{11}, by assuming that the rate of plastic strain is null. Interestingly, since the plastic strain does not appear in the evolution equation of the material velocity v_1 (see Eq. $(13)_1$), the calculation of v_1 will still hold in the presence of plastic deformation. The stress field obtained is called the elastic predictor and will identified by the subscript $(\cdot)_{\text{trial}}$.

2.2.3. Plastic correction

After the computation of the stress field considering an elastic propagation, we must check if the elastic predictor is plastically admissible. If the condition $g(\boldsymbol{\sigma}_{\text{trial}}^{k+1}, R^k) \leq 0$ is met, then the evolution is purely elastic and the final mechanical state is simply given by

$$\begin{cases} \boldsymbol{\sigma}^{k+1} & = \boldsymbol{\sigma}_{\text{trial}}^{k+1} \\ \boldsymbol{\varepsilon}_p^{k+1} & = \boldsymbol{\varepsilon}_p^k, \end{cases} \tag{24}$$

where the stress component $(\sigma_{22}^{k+1})_{\text{trial}}$ is obtained using Eq. (10):

$$(\sigma_{22}^{k+1})_{\text{trial}} = \sigma_{22}^k + \frac{3\kappa - 2\mu}{3\kappa + 4\mu}\left((\sigma_{11}^{k+1})_{\text{trial}} - \sigma_{11}^k\right). \tag{25}$$

However, if $g(\boldsymbol{\sigma}_{\text{trial}}^{k+1}, R^k) > 0$, then the elastic predictor is not plastically admissible and a plastic correction is needed using a radial return algorithm (Simo and Taylor, 1986; Ming and Pantalé, 2018) (for a detailed description see Bonnet and Frangi, 2007) to ensure that the plasticity criterion is verified. In that case, the increment of the plastic strain must be computed using the flow rule and the consistency conditions. Because of the non-linearity of the Johnson–Cook model in Eq. (5), there is no explicit solution to this problem, making it semi-analytic. The final stress can be written as

$$\boldsymbol{\sigma}^{k+1} = \boldsymbol{\sigma}_{\text{trial}}^{k+1} - (3\kappa\mathbb{J} + 2\mu\mathbb{K}) : \Delta\boldsymbol{\varepsilon}_p^k, \tag{26}$$

where $\Delta\boldsymbol{\varepsilon}_p^k$ is the plastic strain increment which is given by

$$\Delta\boldsymbol{\varepsilon}_p^k = \Delta p^k \frac{3}{2}\frac{\boldsymbol{\sigma}_d^{k+1}}{\sigma_{\text{eq}}^{k+1}}. \tag{27}$$

In Eq. (27), Δp^k is the increment of the equivalent plastic strain, which constitutes the unknown of the projection problem. Using Eq. (27), the final stress reads

$$\boldsymbol{\sigma}^{k+1} = \boldsymbol{\sigma}_{\text{trial}}^{k+1} - 3\mu\Delta p^k \frac{\boldsymbol{\sigma}_d^{k+1}}{\sigma_{\text{eq}}^{k+1}}. \tag{28}$$

By taking the von Mises norm of the stress $\boldsymbol{\sigma}^{k+1}$, one gets

$$\sigma_{\text{eq}}^{k+1} = \sigma_{\text{trial,eq}}^{k+1} - 3\mu\Delta p^k. \tag{29}$$

The yield criterion $g(\boldsymbol{\sigma}^{k+1}, R^{k+1}) = 0$ must be verified which leads to:

$$\sigma_{\text{trial,eq}}^{k+1} - 3\mu\Delta p^k - R(p^{k+1}, \dot{p}^{k+1}) = 0, \tag{30}$$

where p^{k+1} and $\dot{p}^{k+1}$ are given by

$$p^{k+1} = p^k + \Delta p^k, \quad \dot{p}^{k+1} = \frac{\Delta p^k}{\Delta t}. \tag{31}$$

Eq. (30) is a nonlinear equation with the sole unknown Δp^k which can be solved using a Newton method. Once Δp^k is known, the final stress can be deduced by combining Eqs. (28) and (29):

$$\boldsymbol{\sigma}^{k+1} = \frac{1}{3}\text{Tr}(\boldsymbol{\sigma}_{\text{trial}}^{k+1})\boldsymbol{I} + \boldsymbol{\sigma}_{\text{trial},d}^{k+1}\left(1 - \frac{3\mu\Delta p^k}{\sigma_{\text{trial,eq}}^{k+1}}\right). \tag{32}$$

$\boldsymbol{\sigma}^{k+1}$ can now be used to compute $\boldsymbol{\varepsilon}_p^{k+1} = \boldsymbol{\varepsilon}_p^k + \Delta\boldsymbol{\varepsilon}_p^k$ with Eq. (27).

The plastic correction is further detailed in the following pseudo-code algorithm.

Algorithm Plastic correction

Input variables: σ_{11}^k, σ_{22}^k, ε_{11}^k, $\varepsilon_{p,11}^k$, p^k, R^k.
Compute $\sigma_{11}^{\text{trial}}$, v_1^{k+1} with the numerical method assuming an elastic propagation with Eq. (23).
Compute the corresponding $\sigma_{22}^{\text{trial}}$ value with Eq. (10).
Elastic trial: $\varepsilon_{p,11}^{k+1} = \varepsilon_{p,11}^k$ and $p^{k+1} = p^k$
if $J_2(\boldsymbol{\sigma}^{\text{trial}}) - R^k \leq 0$ **then**
  $\boldsymbol{\sigma}^{k+1} = \boldsymbol{\sigma}^{\text{trial}}$
else
  Find Δp such that $\sigma_{\text{eq,trial}}^{k+1} - 3\mu\Delta p - R(p^{k+1}, \dot{p}^{k+1}) = 0$
  Compute $\boldsymbol{\sigma}^{k+1} = \frac{1}{3}\text{Tr}(\boldsymbol{\sigma}_{\text{trial}}^{k+1})\boldsymbol{I} + \boldsymbol{\sigma}_{\text{trial},d}^{k+1}\left(1 - \frac{3\mu\Delta p^k}{\sigma_{\text{trial,eq}}^{k+1}}\right)$
  Compute $\Delta\boldsymbol{\varepsilon}_p = \frac{3}{2}\frac{\boldsymbol{\sigma}_d^{k+1}}{\sigma_{\text{eq}}^{\text{trial}}}\Delta p$
  Compute $\boldsymbol{\varepsilon}_p^{k+1}$ and p^{k+1} using $\Delta\boldsymbol{\varepsilon}_p$ and Δp.
  Compute $R^{k+1} = R(p^{k+1}, \dot{p}^{k+1})$
End

2.3. Residual stresses modeling

The resolution of the shock wave propagation permits the determination of the evolution of *residual plastic strain*. However, the residual stresses results from the material reaching a static equilibrium. In other words, the residual stress field has to be determined once there is no more wave propagating in the specimen. It is thus necessary to rely on another procedure to determine the residual stress field. To this end, the residual stress field can be approximated by analytic methods, as presented in the case of thermal strains by Johns (1965). Ahdad and

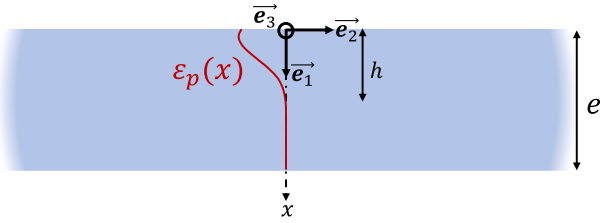

Fig. 2. Illustration of the plate specimen. The red curve symbolizes the typical in-depth distribution of the plastic strain. (For interpretation of the references to color in this figure legend, the reader is referred to the web version of this article.)

Desvignes (1996) applied a similar method for plastic strains for various geometries (see also Korsunsky, 2005; Gelineau, 2018; Cochennec, 2009; Ahdad and Desvignes, 1996; Cellard et al., 2012, 2007). These methods are based on the calculation of the stress equilibrium due to the presence of incompatible internal permanent strains (termed as eigeinstrains) which can be induced by inhomogeneous inelastic deformation, temperature gradients, or phase transformations. The analytic nature of these methods allows a fast computation of the residual stresses.

Therefore, the plastic strain field, generated by the shock wave propagation presented in Section 2, will be used as an initial eigenstrain and the associated residual stress field will be determined from it. In practice, the residual stress field also depends on the thickness of the specimen, and more generally on its geometry.

Here we assume that the specimen is an infinite planar plate free of external loads, and is of finite thickness e, with plastic strains introduced along a thickness h, as illustrated on Fig. 2. In this configuration, the plate is left unconstrained and is free to bend as a result of the static equilibrium. The notation h corresponds to the depth until which LSP generates plastic strain, i.e. $\varepsilon_p(x) = 0$ for $x \geq h$ and thus $\int_h^e \varepsilon_p(x)\mathrm{d}x = 0$. Due to the axisymmetry of the laser shock considered in Section 2, the resulting plastic strain field obtained in the stress wave propagation step is axisymmetric, see Eq. (8). We assume that this plastic strain field is uniform and infinite in the $\boldsymbol{e}_2$ and $\boldsymbol{e}_3$ directions, and thus depends only on x. The total strain tensor is also axisymmetric:

$$\boldsymbol{\varepsilon} = \varepsilon_{11}(x)\boldsymbol{e}_1 \otimes \boldsymbol{e}_1 + \varepsilon_{22}(x)\left(\boldsymbol{e}_2 \otimes \boldsymbol{e}_2 + \boldsymbol{e}_3 \otimes \boldsymbol{e}_3\right). \tag{33}$$

Following Korsunsky (2005) (see also Gelineau 2018 who studied this problem in a more general case), the resolution of the compatibility equations yields that the radial strains in the bent plate are of the following form:

$$\varepsilon_{22}(x) = \varepsilon_{33}(x) = \alpha x + \beta, \tag{34}$$

where α and β are constants to be determined. This result, stemming from the resolution of the compatibility equations, was also used in Cellard et al. (2012) to compute the plastic strains from measured residual stresses. Then, since the plate is infinite in the $\boldsymbol{e}_2$ and $\boldsymbol{e}_3$ directions and the axial stress in zero at the surface, the stress state is planar, so that one has

$$\sigma_{11}(x) = 0, \quad \forall x. \tag{35}$$

This implies that

$$\varepsilon_{11}(x) = -2\frac{3\kappa - 2\mu}{3\kappa + 4\mu}\varepsilon_{22}(x) + \frac{6\mu}{3\kappa + 4\mu}\varepsilon_p(x). \tag{36}$$

Using Eqs. (36), (34) and Eq. $(1)_2$, we obtain:

$$\sigma_{22}(x) = \sigma_{33}(x) = \frac{18\kappa\mu}{3\kappa + 4\mu}\left(\alpha x + \beta + \frac{\varepsilon_p(x)}{2}\right). \tag{37}$$

The constants α and β are determined by enforcing the absence of external force, so that the normal forces and bending moment are at equilibrium. This leads to:

$$\begin{cases} \int_0^e \sigma_{22}(x)\mathrm{d}x = 0 \\ \int_0^e \sigma_{22}(x)x\mathrm{d}x = 0, \end{cases} \tag{38}$$

and similarly for $\sigma_{33}(x)$, not indicated hereafter. Eq. (38) leads to the following system:

$$\begin{cases} 9e\left(\alpha\frac{e}{2} + \beta\right) + \int_0^h \varepsilon_p(x)\mathrm{d}x = 0 \\ 9e^2\left(\alpha\frac{e}{3} + \frac{\beta}{2}\right) + \int_0^h \varepsilon_p(x)x\mathrm{d}x = 0, \end{cases} \tag{39}$$

where the quantity $\varepsilon_p(x)$ is integrated only up to h since $\int_h^e \varepsilon_p(x)\mathrm{d}x = 0$. Using the following notations

$$\Gamma_1 = \int_0^h \varepsilon_p(x)\mathrm{d}x \quad \text{and} \quad \Gamma_2 = \int_0^h \varepsilon_p(x)x\mathrm{d}x, \tag{40}$$

the resolution of system (38) leads to

$$\begin{cases} \alpha = \frac{12}{e^3}\left(\Gamma_2 - \frac{e\Gamma_1}{2}\right) \\ \beta = \frac{2}{e}\left(2\Gamma_1 - \frac{3\Gamma_2}{e}\right), \end{cases} \tag{41}$$

and

$$\sigma_{22}(x) = \sigma_{33}(x) = \frac{18\kappa\mu}{3\kappa + 4\mu}\left(\frac{2\Gamma_1}{e^2}(2e - 3x) + \frac{6\Gamma_2}{e^3}(2x - e) + \frac{\varepsilon_p(x)}{2}\right). \tag{42}$$

Notably, the curvature radius of the plate due to the bending is given by $\Omega = e/\left[6\left(2\Gamma_2 - \Gamma_1\right)\right]$ (see for example Korsunsky 2005). The curvature radius is particularly useful for the residual stresses analysis by Almen strip deflection (Glaser et al., 2022; Miao et al., 2010) (which requires however experimental measurements unlike our approach).

It is worth noticing that for very large thicknesses, i.e. when e tends to infinity, the coefficients α and β from Eq. (41) tend to zero. We thus have $\varepsilon_{22}(x) = 0$ and we obtain the standard result (Ahdad and Desvignes, 1996):

$$\sigma_{22}(x) = \sigma_{33}(x) = \frac{18\kappa\mu}{3\kappa + 4\mu}\frac{\varepsilon_p(x)}{2}. \tag{43}$$

3. Backface velocity simulations

3.1. Presentation of the simulations

The purpose of this section is to assess the model developed in Section 2 through several numerical tests. These numerical results will be notably compared to 3D FE results acting as a reference, to assess the ability of our model to correctly evaluate the mechanical fields, in the case of different material parameters and laser spot diameters for the 3D FE model. We start with a section dedicated to the backface velocity, which is a quantity of interest, because it can be measured experimentally (Peyre et al., 2012). The simulation of the backface velocity only needs the stress propagation step (see Section 2.2). The comparison to a 3D FE model will also allow us to investigate to what extend the 1D model correctly approximates 3D fields.

Material parameters To investigate the performances of the 1D model, various material will be tested. We will consider four materials with a strain-rate dependent behavior: a 12Cr steel, a stainless steel alloy, a titanium alloy and an aluminum alloy. The material parameters are given in Table 1, where E refers to Young's modulus, and ν to the Poisson ratio.

Table 1
Materials parameters for the simulations according to the references listed.

	ρ (kg.m^{-3})	E (GPa)	ν	κ (GPa)	μ (GPa)	A (MPa)	B (MPa)	n	C	$\dot{\epsilon}_0$ (s^{-1})
12Cr Steel (Peyre et al., 2007)	7800	210	0.3	175	80.8	870	400	0.4	0.015	0.01
316L (Umbrello et al., 2007)	7800	210	0.3	175	80.8	305	441	0.1	0.057	1
Ti-6Al-4V (Meyer and Kleponis, 2001)	4500	116	0.34	120.8	43.3	862.5	331.2	0.34	0.012	1
Al7075-T6 (Zhang et al., 2015)	2700	69	0.33	67.6	25.9	473	210	0.3813	0.033	0.01

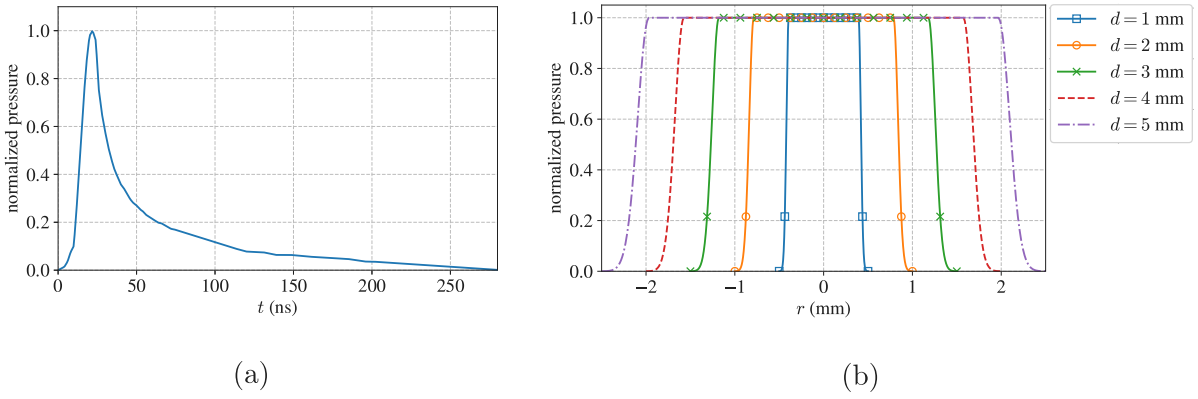

Fig. 3. Laser loading modeling from Le Bras et al. (2019): (a) normalized time pressure profile, (b) normalized spatial pressure distribution for several spot diameters.

Applied loading The applied loading is typical for a laser impact application. We use a temporal and spatial description (adapted from Le Bras et al., 2019) of the pressure applied on the top surface of the specimen, represented in Fig. 3. Fig. 3(b) displays several spatial distributions, corresponding to different spot diameters. The values chosen for those diameters are physical diameters used in experimental conditions, and will be used in the 3D FE model.

For both the 1D and 3D models, we consider a thickness of the specimen of $e = 0.5$ mm to mimic standard experimental conditions, a pressure amplitude of $P = 5$ GPa in order to properly observe plastic effects in the backface velocity results, and a total simulation duration of 400 ns.

Description of the 1D model For the 1D modeling, we impose $\Delta x = 2$ μm for the spatial increment, which is a value for which convergence is reached, and a CFL value of 0.9, leading to values of Δt of approximately 0.3 ns. The used boundary conditions are:

$$\sigma_{11}(0,t) = P(t) \quad \text{and} \quad \sigma_{11}(e,t) = 0, \tag{44}$$

where $P(t)$ refers to the time pressure profile (see Fig. 3(a)). According to Ballard (1991) (see also Ballard et al., 1991; Heuzé, 2017), the hydrodynamic behavior of the specimen can be neglected when the maximum value of the pressure is smaller than 0.1κ, which is satisfied for all the materials in Table 1. In that case, the small strains approximation is valid. Moreover, the initial conditions are:

$$\begin{cases} \sigma_{11}(x,0) = 0 \\ v_1(x,0) = 0 \end{cases} \quad \text{for} \quad 0 \le x \le e. \tag{45}$$

Description of the finite element model For the finite element modeling, we follow the strategy of Seddik et al. (2022), and use an axisymmetric model with the commercial code ABAQUS. The model is illustrated in Fig. 4. We set $L = 7$ mm, which is large enough not to influence the results. This geometry is chosen in order to mimic experimental conditions. The spatial distribution of the applied pressure follows the profiles of Fig. 3(b) for the various spot diameters d, which are taken and adapted from Le Bras et al. (2019). CAX4R elements of dimensions 2 μm × 2 μm are used. The results are achieved with an ABAQUS/Explicit analysis step lasting 400 ns, which is long enough for the axial wave to travel back and forth several times. Still in order to replicate the experimental setup, a unique zero-displacement and zero-rotation boundary condition is enforced at the location of point A in Fig. 4. The backface velocity corresponds to the axial velocity taken at point O.

3.2. Backface velocity results

We present the results for the backface velocity in Fig. 5 for the four materials of Table 1.

The results of Fig. 5 show the evolution on the backface velocity of point O in Fig. 4. Only the results for the diameters $d = 1$ mm, $d = 3$ mm and $d = 5$ mm were presented to keep Fig. 5 clear. The results for diameters $d = 2$ mm and $d = 4$ mm are intermediary to their respective adjacent diameters. Each "principal" peak in Fig. 5 represents the axial wave being reflected at the back face. The time separating the large peaks corresponds to the time necessary for the wave to go back and forth in the specimen. Fig. 5 shows that for all materials, the larger the spot size, the longer the 1D model perfectly captures the behavior of the 3D model. An excellent match is obtained for approximately 120 ns for $d = 1$ mm, and up to 350 ns for $d = 5$ mm. For all materials, the first peak exhibits a slight change of curve at approximately 100 ns. This is called the elastic precursor, and corresponds to the lowest value of velocity above which the wave induces plasticity. It is caused by a change of wave velocity, which is higher when the stress wave is elastic than when it is plastic. For all material and spot sizes, after a while, edge effects (Berthe et al., 2011; Ecault et al., 2016; Ayad et al., 2022) start to appear, thus causing discrepancies. These edge effects are due to waves originating from the laser spot edges and propagating inward, and thus this perturbation arrives quicker at the center for smaller spot sizes. Therefore these perturbations depend mainly on the spot size but also on the plate thickness and the material. Overall, the approximate 1D model proposed is suitable to describe the elastic–plastic stress wave propagation apart from edge effects, and yields excellent results for large spot sizes ($d \ge 5$ mm). More specifically, an excellent agreement was observed for a large spot diameter of 15 mm (in this case we used $L = 15$ mm) for the whole duration of the simulation, but the

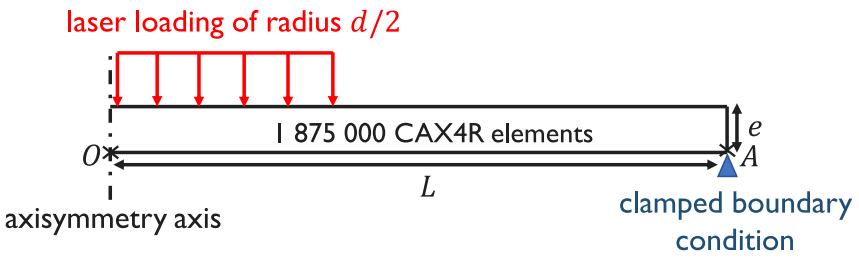

Fig. 4. Illustration of the FE model used for the backface velocity simulations.

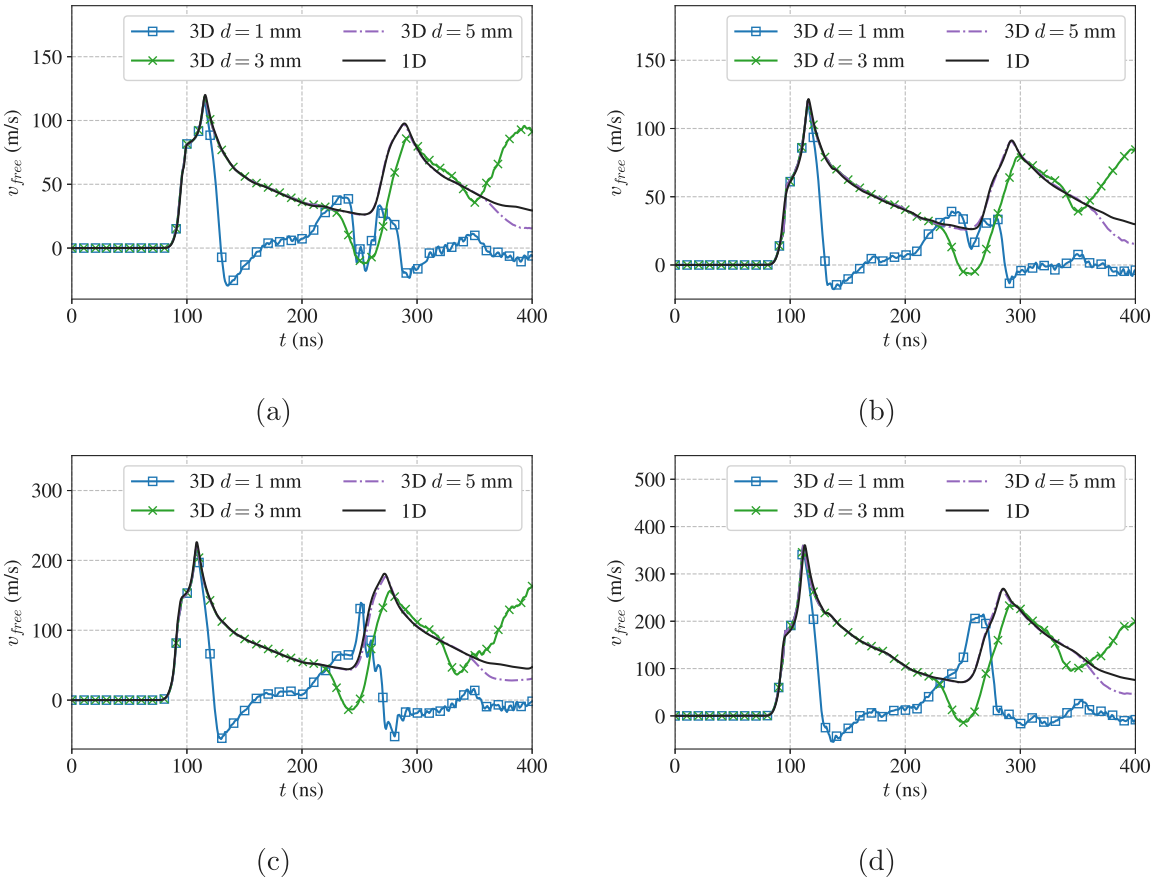

Fig. 5. Comparison of the backface velocity simulations between the 1D model and 3D FE reference solution for the different materials and three laser spot sizes. (a) 12Cr, (b) 316L, (c) Ti-6Al-4V and (d) Al7075-T6.

corresponding results are not presented for the sake of conciseness and since such large spot sizes hold little physical meaning, because they are unrealistic for current LSP configurations. An approximate critical time above which the results from the 1D and 3D models are expected to differ can be expressed as:

$$t_c = \frac{d}{2}\sqrt{\frac{3\rho}{3\kappa + 4\mu}}, \tag{46}$$

which corresponds to the time a compression/traction wave takes to travel from the laser spot edges to the center of the impact at the surface. Therefore, for a given spot size, the 1D model can be used for the identification of the constitutive relation for any time t such that $t < t_c$. To quantify further the performance of the 1D model, we can compute the average relative errors obtained for the backface velocity profiles between the 1D and 3D models for the different materials and spot diameters used in the simulations. The errors are calculated with the parts of the results such that $t \leq t_c$, since this is the condition we have identified for the 1D model to be relevant. It is worth noting that the backface velocity is extremely well reproduced by the 1D model, the average error between the 1D and the 3D FE models being smaller than 2% up to the critical time t_c for all materials and spot diameters. When calculating the same errors for $t \leq 400$ ns (i.e. for the whole duration of the simulations), they are of the order of 21.5% for $d = 1$ mm, 10% for $d = 2$ mm, 6.8% for $d = 3$ mm, 2.2% for $d = 4$ mm and 1.3% for $d = 5$ mm. It must be noted that this critical time t_c is not an exact value but only an approximation. Finally, to give an estimation of the CPU time that can be expected to obtain such results, converged computations with the 1D model are generally 10 times faster than with the 3D model with the parameters considered.

4. Residual fields induced by the stress wave propagation

4.1. Presentation of the simulations

Now that the performance of the propagation scheme is validated until a critical time that depends on the spot size, we focus on the residual fields generated by the propagation of a stress wave, more precisely

Table 2
Mesh sizes considered for the FE calculations.

	$d = 1$ mm	$d = 2$ mm	$d = 3$ mm	$d = 4$ mm	$d = 5$ mm
L (mm)	2	4	6	8	10
mesh size (μm × μm)	5 × 5	10 × 10	10 × 10	10 × 10	10 × 10

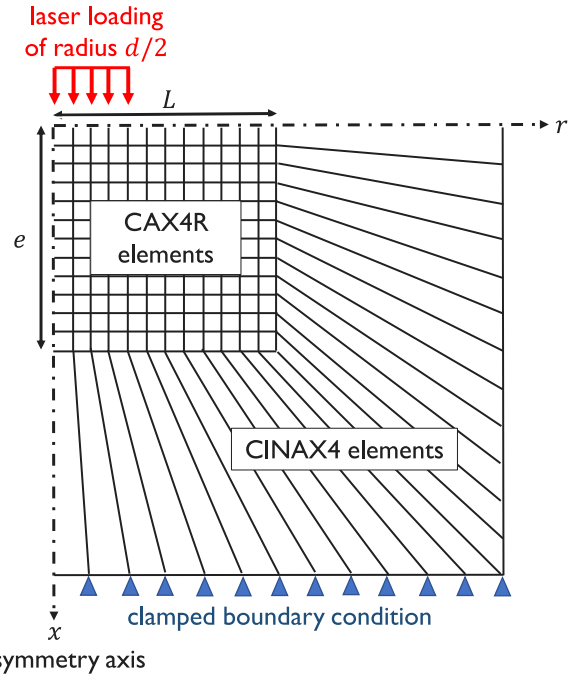

Fig. 6. Representation of the FE model used for the residual stress field simulations. The size of the represented mesh is only for illustrative purposes, not to scale.

the residual plastic strains and residual stresses. The developments of Section 2 will be here again compared to a 3D model for various laser spot sizes and materials already indicated in Section 3.1. Since we are simulating the LSP process, a change of configuration is necessary.

Description of the 1D model For the 1D model, the thickness e is 10 mm, the spatial increment is $\Delta x = 5$ μm, so that the computations have reached convergence while keeping the size of the model reasonable. The CFL number is set to 0.9. Again, the laser loading keeps only the time pressure profile from Fig. 3(a), with a pressure amplitude of 3 GPa (which is also under 0.1κ allowing us to neglect the hydrodynamic behavior Ballard, 1991; Ballard et al., 1991, keeping the deformation small).

The boundary conditions are similar to the ones used for the back face velocity simulations of Section 3.1: the boundary conditions for $\sigma_{11}(0,t)$, $\sigma_{11}(x,0)$ and $v_1(x,0)$ are the same as in Eq. (44) and Eq. (45). The residual stress field can be computed once the total kinetic energy in the specimen has vanished. To reach this state in the simulation, we enforce non-reflective boundary conditions, to avoid reflection of the stress wave at the boundary. To that end, we use a zero-order extrapolation (Leveque, 2002) of the unknowns at the boundary $x = e$:

$$\begin{cases} \sigma^k_{11,N} = \sigma^k_{11,N-1} \\ v^k_{1,N} = v^k_{1,N-1} \end{cases} \tag{47}$$

Description of the finite element model For the FE reference solution, we follow the methodology of Morin et al. (2021). The geometry is divided into two zones, as illustrated in Fig. 6: (i) a central rectangular zone of dimension $e \times L$ mm meshed with CAX4R elements in which we will study the mechanical fields; (ii) an outer zone meshed with infinite CINAX4 elements which ensure that there is no stress wave reflection.

It should be noted that the mesh represented in Fig. 6 does not represent the actual mesh, which is too fine to be clearly presented. The analysis is made with a unique ABAQUS/Explicit step (Peyre et al., 2012, 2007) with a total duration of 20 μs, so that the relaxation can occur, and so that the kinetic energy of the system reduces to a small fraction of its original value. Clamped boundary conditions are applied on the bottom edge of the model. The maximum pressure applied is $P = 3$ GPa, the time profile remaining the same as in Fig. 3.

Since plasticity will not be induced on the same surface size for all the test cases, the number of elements leading to converged results for the residual fields will not be the same as well. Thus, for each spot diameter, the FE results will be presented for a mesh producing converged results. Besides, to avoid models with a too large number of nodes, the width L of the finely meshed box will also vary. It has been verified that the residual stress field results show no variations for a ratio L/d of 2 or greater, d denoting the spot diameter. The parameters are summarized in Table 2.

4.2. Results

4.2.1. Plastic strain field

In this section we analyze the plastic strain field. To do so, a section of the 3D results is first presented, as well as a map of the relative error between the 3D and the 1D results. As explained above, the 1D results do not depend on r unlike the 3D FE results. The relative error map is computed by comparing the in-depth profiles from both models, at the different distances r from the center for the 3D model. These maps will only be presented in the case of the 316L material, for the sake of conciseness (see Fig. 7). Similar results are obtained for the three other materials.

Fig. 7(a) shows the axisymmetric axial plastic strain field for the 3D FE model, in the case the 316L alloy and for a spot diameter of $d = 5$ mm. In this case, it is observed that the plastic strain field of the FE reference solution varies only along the depth x in a large radial domain (for r between 0.3 and 2 mm). In this volume, the fields are close to be uniaxial, and resemble the ones computed with the 1D model. This is underlined by Fig. 7(b), in which the relative error between both models is at its lowest in this area, with values smaller than 20%. This is however not true for $0 \leq r \leq 0.3$ mm, and for $r > 2$ mm. Indeed, the large plastic strain at the center of the impact is caused by radial waves originating at the edges of the laser spot, propagating inward and combining themselves at the center, causing the material to reach plasticity again in this area after the first plastic strains caused by the main axial wave, as pointed out by Ding and Ye (2006b). These authors suggest that an unsymmetrical laser spot shape would avoid those effects, which has been verified in the case of a square spot (Cao et al., 2011; Kim et al., 2014; Ding, 2003). Additionally, the area beyond $r > 2$ mm corresponds to the decrease in the pressure spatial profile (see Fig. 3(b)). It is thus no longer high enough to induce plasticity, so the plastic strains decrease. Hence these results suggest that the 1D model can be compared to the 3D FE in the domain $0.3 \leq r \leq 2$ mm, which make approximately 60% of the laser spot size. In the following we compare the 1D results to the 3D results for values taken at $r = d/4$. The residual strain profiles (as a function of the depth) are represented in Fig. 8 for the four materials considered.

The results from Fig. 8 show that the axial plastic strain obtained with the 1D approximation and with the 3D FE model at $r = d/4$ are close to identical for all the materials considered. The plastic strains at the surface $x = 0$ mm are correctly approximated by the 1D model, as well as the plastically affected depth. In this area of the impact,

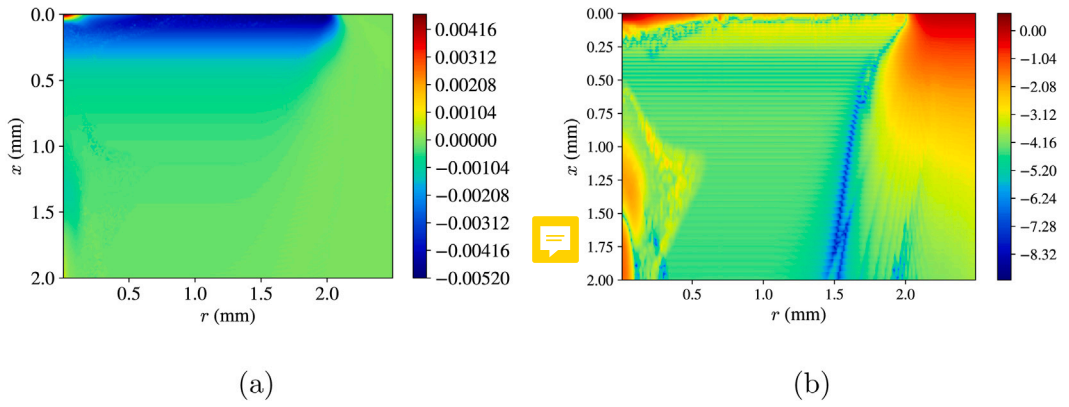

Fig. 7. Distribution of the residual plastic strain in the case of the 316L steel for the 5 mm spot size. (a) 3D FE reference solution and (b) Logarithm ($\log_{10}$) of the relative error between the 1D model and the 3D model.

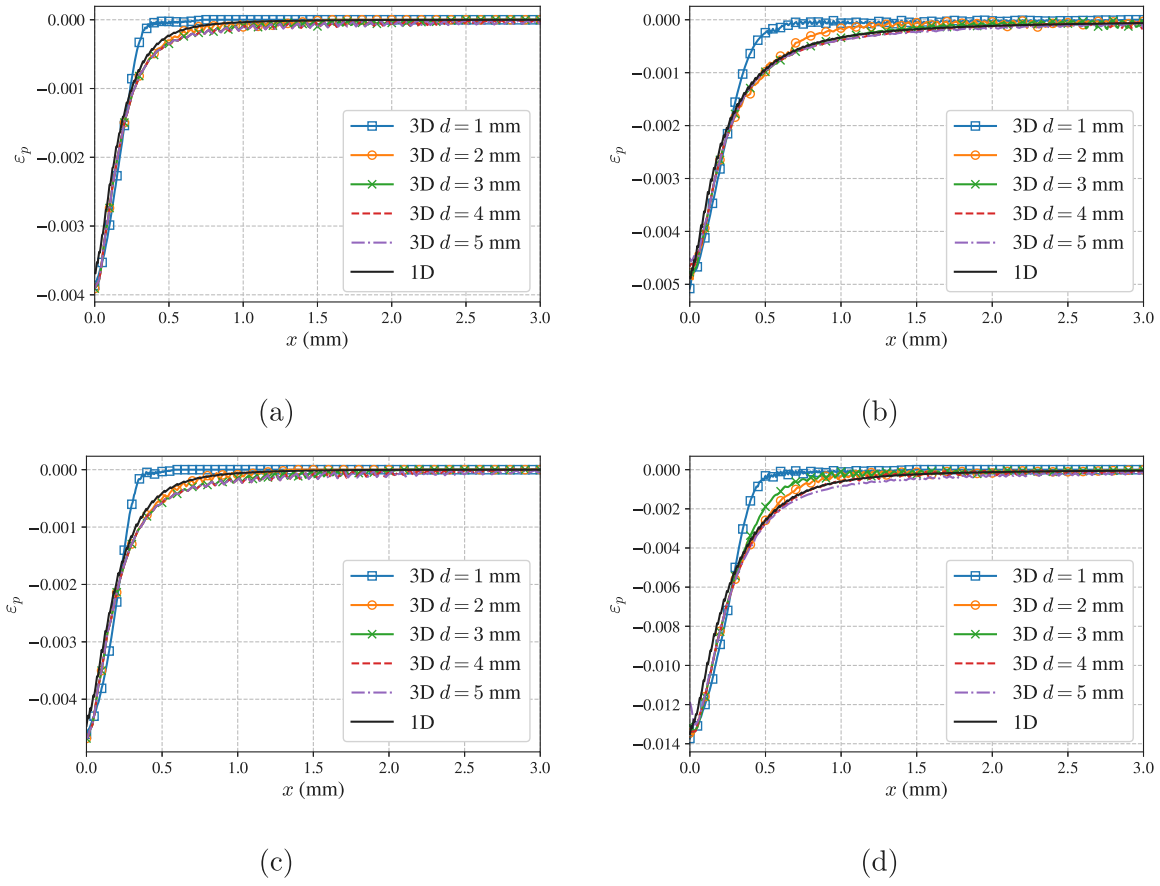

Fig. 8. Comparison of residual axial plastic strain between the 1D (using the plate approximation) and 3D models. The 3D results are for $r = d/4$. Various spot diameters are shown. (a) 12Cr, (b) 316L, (c) Ti-6Al-4V and (d) Al7175-T6.

the spot diameter has little influence on the plastic strain field, except for the 1 mm diameter spot for which some slight differences between the models are observed. It was checked that these differences for the 1 mm diameter are not linked to the mesh size, as a mesh of 2 μm × 2 μm yielded the same results. This apparent size effect is related to the applied pressure whose temporal profile is identical for all test cases: the wavelength of the stress wave being constant, a modification of the spot size can lead to different behaviors. The mean relative errors between the 1D and 3D models for the plastic strains profiles for the different materials and spot sizes are summarized in Table 3.

From these results, it can be considered (empirically) that the 1D model is a good estimate of the 3D model when the spot diameter used is such that

$$d > 2L_p, \tag{48}$$

Table 3
Average relative errors (in %) between the 1D and 3D plastic strains profiles for the different materials and spot sizes, calculated for 0 mm ≤ $x \leq 10$ mm.

	1 mm	2 mm	3 mm	4 mm	5 mm
12Cr	5.6	2.8	3.6	3.7	3.7
316L	6.1	2.5	1.2	1.3	1.5
Ti-6Al-4V	7.2	2.6	3.7	3.8	3.8
Al7075-T6	5.6	1.9	2.7	1.3	2.3

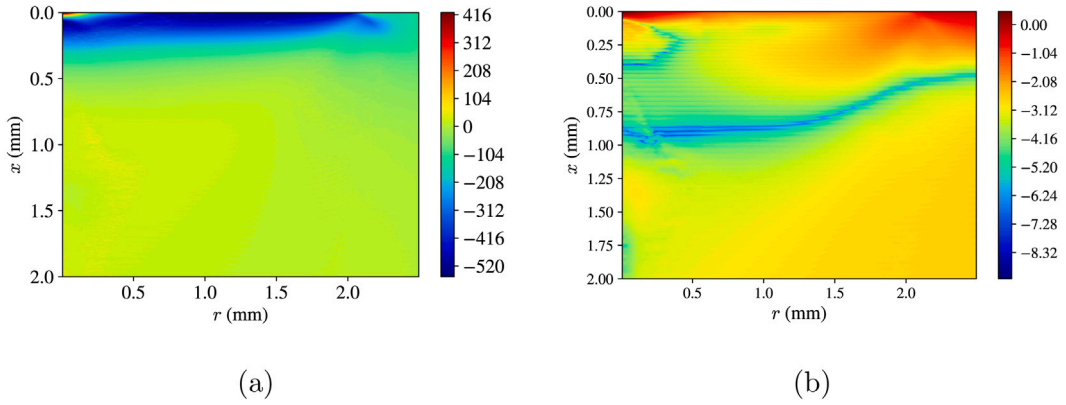

Fig. 9. Distribution of the residual stresses in the case of the 316L steel for the 5 mm spot size. (a) 3D FE reference solution (σ_{22} in MPa) and (b) Logarithm ($\log_{10}$) of the relative error between the 1D model and the 3D model.

where L_p is the plastically affected depth defined by Ballard (1991) (see also Ballard et al., 1991; Heuzé, 2017) in the case of an elastic perfectly plastic material subjected to a step function loading of duration τ:

$$L_p = \frac{cc_p\tau}{c - c_p}\left\lfloor \frac{6\mu P + A(4\mu + 3\kappa)}{2A(4\mu + 3\kappa)} \right\rfloor. \tag{49}$$

In Eq. (49), A is the yield strength of the material, $\lfloor\cdot\rfloor$ is the floor function, c is the elastic stress wave velocity (see Eq. (18)) and c_p is the plastic stress wave velocity in an elastic perfectly plastic material given by:

$$c_p = \sqrt{\frac{\kappa}{\rho}}. \tag{50}$$

In our case the loading is not a step function, but the duration of the time profile of Fig. 3(a) is approximately 20 ns, so Eq. (49) is to be used with $\tau = 20$ ns. The criteria of Eq. (48) was checked for all spot diameters and materials displayed in Fig. 8.

4.2.2. *Residual stress field*

We continue with the study of the residual stresses. First, we investigate the distribution of the residual stress field in the 3D FE reference solution (see Fig. 9) in the case of the 316L steel. Similar results are observed for the other materials.

As for the residual plastic strain field (Fig. 7) it is observed in Fig. 9(a) that the residual stress field of the FE reference solution vary only along the depth x in a large domain (0.3 mm $\leq r \leq$ 2 mm). This is also confirmed by Fig. 9(b), showing that the relative error between the 1D model calculated using Eq. (37) and the 3D model is the lowest in the corresponding area. This is also in this area that the error is the lowest for surface values. Following the trend of the plastic strains field, the center of the impact at the surface shows a singular concentration of residual stresses, up to 0.3 mm, because of the plasticity induced by the radial waves converging in the center after the main axial wave, as reported by Ding and Ye (2006b). As the distance from the center increases, residual stresses tend to zero, starting from 2 mm. In the following, Eq. (37) is used to compute the residual stress field from the plastic strain distribution (shown in Fig. 8) in the 1D model. The results of the 1D model will be compared to the 3D FE reference solution at $r = d/4$ (see Fig. 10).

Overall, a good agreement between the 1D and 3D models is observed for the residual stress profile. The surface residual stresses are generally well reproduced, especially in the cases of the 12Cr (Fig. 10(a)) and the Ti-6Al-4V (Fig. 10(c)) materials. For the 316L and Al7075-T6 materials, the comparison improves when the spot size increases, and an almost perfect comparison is achieved for a spot diameter greater than 9 mm (not shown in Fig. 10). The affected depth by the compressive residual stresses is also correctly approximated, with a maximal error of approximately 0.1 mm. Because of the form

Table 4
Average relative errors (in %) between the 1D and 3D residual stresses profiles for the different materials and spot sizes, calculated for 0 mm $\leq x \leq$ 10 mm.

	1 mm	2 mm	3 mm	4 mm	5 mm
12Cr	3.7	3.4	3	2.7	2.4
316L	5.3	4.8	4.5	4.1	3.8
Ti-6Al-4V	4.3	3.9	3.5	3.1	2.8
Al7075-T6	5.7	5.1	4.8	4.5	3.9

the residual stress field with the thin plate hypothesis from Eq. (37), the residual stresses decrease linearly once the plastic strain has reached zero, whereas the results from the FE model decrease to zero more rapidly after having reached a maximum. However some discrepancies are observed when the spot diameter decreases, in contrast with the plastic strains, for which the match was equally good for all spot diameters larger than 2 mm. Here again, the average relative errors between the 1D and 3D models for the residual stresses profiles for the different materials and spot diameters are presented in Table 4.

These results show that the 1D model can provide a good approximation of 3D mechanical fields. In the following sections, we will discuss the performance of the 1D model under different parameters.

5. Discussion

The results from Sections 3 and 4 showed that the 1D model developed in Section 2 is able to successfully reproduce 3D FE reference results for typical parameters involved in LSP processing. In this discussion, we wish to investigate the effect of the specimen thickness and the influence of the pressure on the ability of the 1D model to correctly compute the residual mechanical fields.

Influence of the thickness The results from Figs. 8 and 10 have shown that the 1D model developed in this paper can provide a correct approximation of the residual mechanical fields after the propagation of the stress wave. The results were presented for the same thickness along which residual stresses reach equilibrium, i.e. 10 mm. We wish to discuss the sensitivity of the results on the thickness, by performing simulations with thicknesses of $e = 3$ mm and $e = 20$ mm. The ratio h/e with h and e defined in Fig. 2 is thus different. Since the results of Figs. 8 and 10 showed that the spot diameter has little influence on the results for large laser spots, the following results will be presented for a spot diameter of 5 mm. Furthermore, results will only be presented in the case of the 316L steel, the conclusions drawn from it being similar for the other materials.

Fig. 11(a) shows a comparison of the axial plastic strains between the FE and 1D models for two different thicknesses. The results are presented as functions of the depth normalized against the thickness.

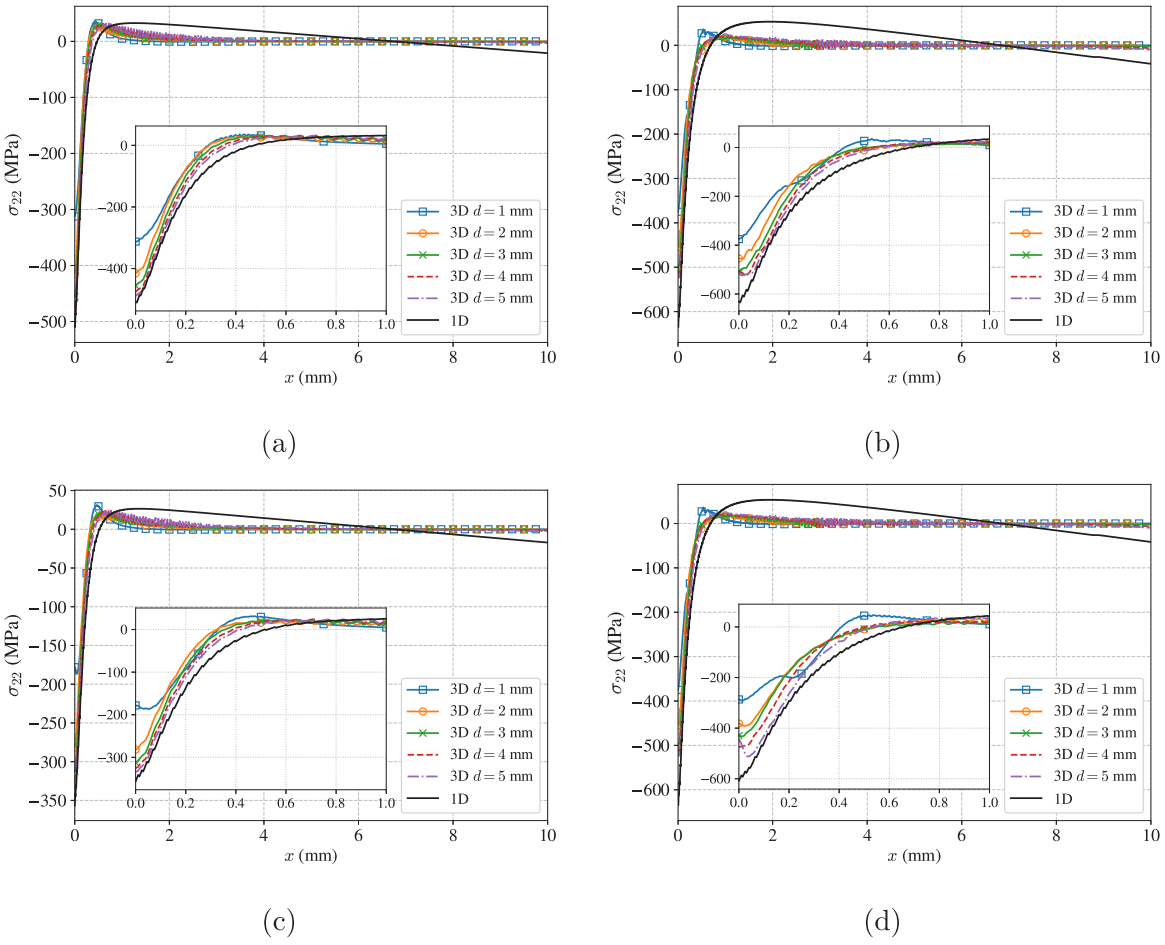

Fig. 10. Comparison of residual stresses between the 1D (using the plate approximation) and 3D models. The 3D results are for $r = d/4$. Various spot diameters are shown. The inserted figures show zooms for $r \leq 1$ mm of the corresponding results. (a) 12Cr, (b) 316L, (c) Ti-6Al-4V and (d) Al7175-T6.

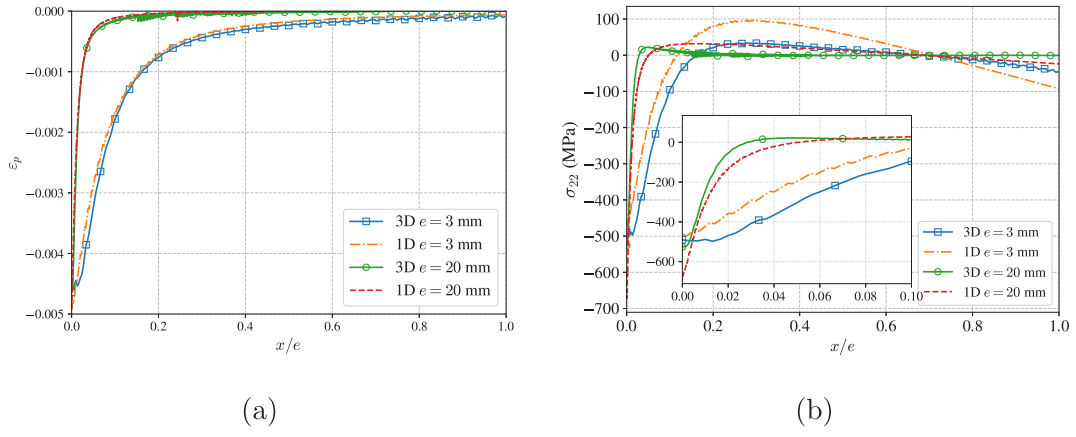

Fig. 11. Comparison between the 3D FE (for a spot diameter of 5 mm) and 1D models, with thicknesses of 3 mm and 20 mm, for the 316L steel. (a) Residual plastic strains and (b) Residual stresses.

As in the case of $e = 10$ mm (Fig. 8), the 3D axial plastic strains at mid-radius are very well approximated by the 1D model for both the 3 mm and 20 mm thicknesses. Since there is no variation of geometry in the plastically affected zone, and since the plastic strains only depend on the load amplitude, it is expected to obtain similar results for the tested thicknesses. Contrary to the plastic strains, the residual stress field is sensitive to the geometry of the specimen, since it must be at equilibrium over all the specimen. Hence, the residual stress profiles of Fig. 11(b) are different between the 3 mm and 20 mm thicknesses.

According to Fig. 11(b), the overall comparison between the 3D and 1D models remains good for the 20 mm thickness, with a correct approximation of the affected depth as well as the surface residual stresses. However, the 3 mm thickness does not yield a similar comparison. Indeed, since the coefficients α and β from Eq. (41) are greater for a smaller thickness than a larger one, the results for the case $e = 3$ mm are shifted toward smaller stress values compared to the results of the case $e = 20$ mm, which makes the 1D model overestimating the 3D FE model in the 20 mm case, and underestimating it for the 3 mm case.

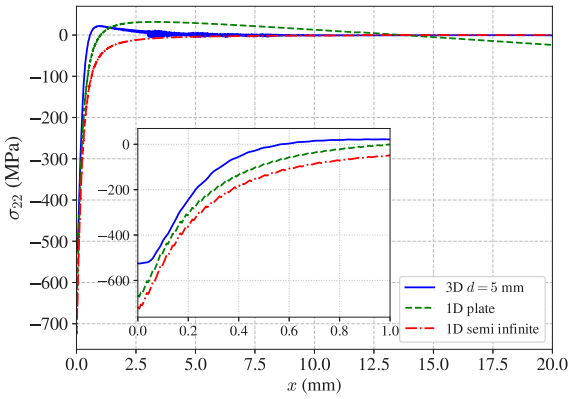

Fig. 12. Comparison of the residual stresses between the 3D FE (for a spot diameter of 5 mm) and 1D models, with the infinitely planar and semi infinite specimen hypotheses, for the 316L material.

For all the materials, the average absolute error between the 1D and 3D results is about twice as much for the 3 mm thickness (∼ 20 MPa) than for the 20 mm thickness (∼ 10 MPa).

In addition, in the case $e = 20$ mm, it can be interesting to use the semi infinite specimen approximation of Eq. (43). Fig. 12 presents a comparison between the residual stresses obtained by the 1D models, with infinitely planar (with a thickness of 20 mm) and semi-infinite approximation, and with the 3D FE model for a spot diameter of 5 mm. These results show that for this thickness, the infinite plate and semi infinite specimen hypotheses are close for the first hundreds of microns, with notably very close values for the surface residual stresses. However, the affected depth by the compressive residual stresses is overestimated by the semi infinite specimen hypothesis for all materials (which does not capture the tensile residual stresses due to the equilibrium, even though these stresses are small). The far field of the reference solution, which is zero, is more correctly approximated by the semi infinite specimen hypothesis. However, the slope and values of the infinitely planar solution in the far field are such that this solution is also close to zero. For these reasons, the infinitely planar hypothesis remains a good approximation for large thicknesses, while the semi-infinite specimen hypothesis is relevant for very large thicknesses.

Influence of the pressure In this paragraph, we wish to discuss its sensitivity to the applied pressure. We will thus consider now an amplitude of 5 GPa, instead of the previous 3 GPa. All the other parameters will be identical to the ones used in Section 4. The results will be only presented for the 316L steel, the conclusion being similar for the other materials.

Fig. 13 presents the comparison between the 1D and 3D models for the plastic strains and residual stresses. The trend of the results is similar to Figs. 8 and 10, but with some differences. The plastic strains in Fig. 13 for spot diameters from 3 mm to 5 mm and the 1D results exhibit a saturation plateau close to the surface, which was absent of the profiles in Fig. 8. Interpretations for the phenomena can be found in the work of Ballard (1991), who explains, in the ideal case of an elastic perfectly plastic material, that above a given pressure amplitude, plasticity will not only be induced during the loading front of the shockwave, but also during the release front of the wave (when the axial stress is decreasing), resulting in a saturation plateau, whose value depends only on the material parameters. Moreover, the value of the plateau in the FE results seems to be affected by the spot diameter, becoming closer to the 1D model as the spot diameter increases. Furthermore, specimen undergoes softening during the unloading phase of the pressure wave, as the equivalent plastic strain p continues to rise, but its rate $\dot{p}$ decreases, due to the fact that the pressure time profile in Fig. 3(a) is not symmetric, thus leading to a yield stress lower that the one achieved during the loading phase of the shock, according to the Johnson–Cook model given by Eq. (5). As the stress wave is attenuated during the propagation, there is a transition between the zone where plasticity is induced only by the loading phase, and the zone where the unloading also induces plasticity. This transition is marked on Fig. 13 at $x \sim 0.25$ mm, where the plastic strain and residual stress profiles exhibit a sharp evolution. This saturation plateau corresponds to the softened part of the specimen, explaining the behavior in the residual fields profiles. Furthermore, as previously, the larger the spot size, the better the comparison between the 1D and 3D models is. The surface residual stresses are overestimated for small spot sizes, but the stress profile is well approximated, as well as the affected depth. These results seem to indicate that for high pressures, the 1D model can again approximate precisely the FE reference solution, but for large spot sizes. For the results of Fig. 13, additional simulations have shown that a better agreement of the surface values are is achieved for a laser spot of 15 mm. The profiles of Fig. 13 can also be used to check the criteria of Eq. (48).

As for the CPU times required by both models to complete the computations, the 1D algorithm is significantly faster. It should be noted that the computational time can be influenced by the type of materials since (i) a material with a low yield strength will need more plastic correction steps (which take longer than the purely elastic propagation computation) and (ii) the CFL condition of Eq. (16) must hold at all times so a material with a faster propagation speed will need a smaller time increment (for a given CFL number and spatial increment), and thus a longer time to complete the simulation. Overall, for the residual fields with the current parameters, the 1D model is approximately 40 times faster than the 3D model.

6. Conclusion

The present work aimed at providing a 1D model to achieve a fast approximation of the mechanical fields induced by a stress wave caused by a laser impact during the Laser Shock Peening process. This model is based on a stress wave propagation step, which generates plastic strains, which are then used to compute the residual stress field using a eigenstrain-based method. The modeling for the propagation step is based on a uniaxial strain hypothesis, which corresponds to the behavior of the material for very large laser spot sizes, with no description of stress wave phenomenon originating from the spot edges. The propagation step is computed by solving a hyperbolic PDE system with a Godunov-type numerical scheme. This propagation step generates a heterogeneous plastic strain field, which is the origin of the residual stress field. An analytic modeling based on an infinitely planar plate allows to link the plastic strains to the residual stresses. To assess the relevance of this model, we compared it to a Finite Element model, acting as a reference solution, for several materials and spot diameters. The stress wave propagation step is validated by comparing the backface velocity of a thin plate impacted on the opposed face between the 1D model and the reference FE solution. For all materials, the match is close to perfect for large spot sizes, preventing edge effects from quickly disturbing the velocity field along the center of the impact. Another dedicated FE model is used to compare the residual plastic and stress fields. It highlights that these fields are uniaxial for the most part of the laser spot, except for the edges, and the center of the impact, which is a locus of additional plastic evolution in the case of circular laser spot shape, because of radial stress waves originating at the edges, propagating inward and focusing at the center of the impact. Apart from these areas, the 1D model yields a very satisfactory approximation of the plastic strains field compared to the FE model, again for the large spot sizes. For the residual stresses, several discrepancies are introduced by the analytic modeling, but the 1D model remains a good approximation for spot diameters larger than 2 mm. Additional tests showed that the 1D model remains relevant for large thicknesses (from 10 mm and higher), but less so for small thicknesses (around

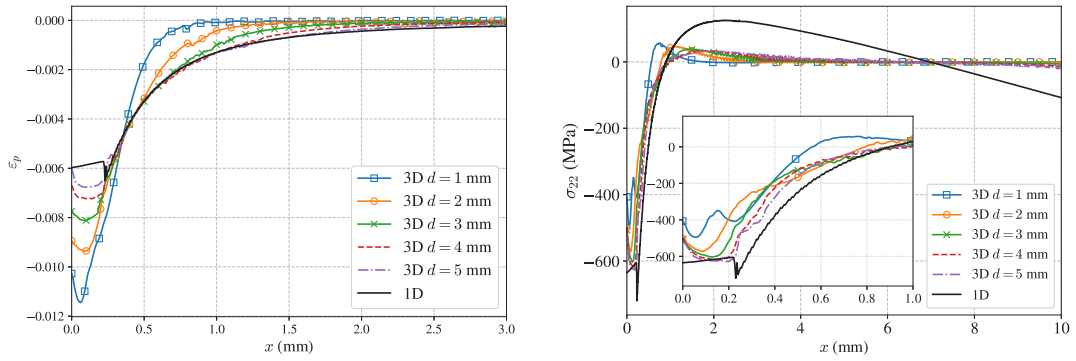

Fig. 13. Comparison of the residual fields between the 1D and 3D models for a pressure amplitude of 5 GPa for the 316L material. (a) Axial plastic strain and (b) Residual stresses.

3 mm). These results suggest that the 1D model can be used to compute a first approximation of the mechanical fields introduced by a laser impact. Such an approximation is quicker to be computed, with the 1D model being on average one or two orders of magnitude faster (this however strongly depends on the machines used, as well as the parallel computing options). This work opens the following perspectives:

- For a material whose behavior is already known, the 1D model could be used to have an initial estimation of the induced residual stress field, before refining the results with more complex models. The 1D model could thus be used to perform an initial optimization of the process parameters.
- In the case where the material parameters are unknown, this 1D model can be efficiently used as a calibration tool. Indeed, even though the Johnson–Cook model has only a few parameters, their identification can be cost and time consuming when using 3D FE simulations (Ayad et al., 2022; Milani et al., 2009; Seddik et al., 2022). Based on proper experimental measurements (backface velocity or in-depth residual stresses) for a material with unknown properties, the 1D model can be used to quickly identify the rheological parameters used to describe the strain rate dependent behavior of the material.
- The thermal effects in the Johnson–Cook model were neglected in this work. However, literature works (Rubio-González et al., 2006; Gill et al., 2015) have shown that the absence of sacrificial overlay protecting the sample from thermal effects can lead to a strong influence of the temperature on the residual stresses, which are less compressive than without thermal effects. An improvement of the model developed in this article would be to include a modeling of the temperature evolution inside the sample given an specific thermal loading, and its influence of the mechanical behavior. This would affect the yield stress and thus the stress wave propagation, and generate eigenstrains of thermal origin, changing the distribution of the residual stresses.

The 1D model presented in this work is made freely available online in the form of a python code called EVEREST (strEss waVE pRopagation and rESidual STress solver) under LGPL license (Lapostolle, 2022). The use of this code only requires a Python installation and standard scientific packages, and thus no commercial software or knowledge of finite elements modeling. Its use and results are thus faster than finite elements codes.

Declaration of competing interest

The authors declare that they have no known competing financial interests or personal relationships that could have appeared to influence the work reported in this paper.

Data availability

The code used for the research has been shared at https://github.com/llapo/EVEREST

Acknowledgments

This research was partly funded by the Carnot Institute ARTS and by the French Agence Nationale de la Recherche (ANR), research project ForgeLaser (grant number: ANR-18-CE08-0026).

References

Achintha, M., Nowell, D., 2011. Eigenstrain modelling of residual stresses generated by laser shock peening. J. Mater Process. Technol. 211, 1091–1101.

Achintha, M., Nowell, D., Shapiro, K., Withers, P., 2013. Eigenstrain modelling of residual stress generated by arrays of laser shock peening shots and determination of the complete stress field using limited strain measurements. Surf. Coat. Technol. 216, 68–77.

Adu-Gyamfi, S., Ren, X., Larson, E.A., Ren, Y., Tong, Z., 2018. The effects of laser shock peening scanning patterns on residual stress distribution and fatigue life of AA2024 aluminium alloy. Opt. Laser Technol. 108, 177–185.

Ahdad, F., Desvignes, M., 1996. Contraintes résiduelles et déformations plastiques: Leurs relations mutuelles pour des pièces de géométrie simple. Mater Tech. 84, 46–50.

Amarchinta, H.K., Grandhi, R.V., Langer, K., Stargel, D.S., 2009. Material model validation for laser shock peening process simulation. Modelling Simulation Mater. Sci. Eng. 17, 015010.

Ayad, M., Lapostolle, L., Rondepierre, A., Le Bras, C., Scius-Bertrand, M., Ünaldi, S., Trdan, U., Rouchausse, Y., Grassy, J., Maillot, T., Lapoujade, V., Michel, C., Berthe, L., 2022. Modeling of multi-edge effects in the case of laser shock loadings applied on thin foils: Application for material characterization of aluminum alloys. J. Appl. Phys. 131, 095902.

Ballard, P., 1991. Contraintes résiduelles induites par impact rapide. Application au choc laser (Ph.D. thesis). Ecole Polytechnique.

Ballard, P., Fournier, J., Fabbro, R., Frelat, J., 1991. Residual stresses induced by laser-shocks. Le J. de Phys. IV 01, C3–487–C3–494.

Berthe, L., Arrigoni, M., Boustie, M., Cuq-Lelandais, J.P., Broussillou, C., Fabre, G., Jeandin, M., Guipont, V., Nivard, M., 2011. State-of-the-art laser adhesion test (LASAT). Nondestruct. Test. Eval. 26, 303–317.

Bonnet, M., Frangi, A., 2007. Analyse des solides déformables par la méthode des éléments finis. In: Les éditions de L'école Polytechnique Edition.

Braisted, W., 1999. Finite element simulation of laser shock peening. Int. J. Fatigue 21, 719–724.

Brockman, R.A., Braisted, W.R., Olson, S.E., Tenaglia, R.D., Clauer, A.H., Langer, K., Shepard, M.J., 2012. Prediction and characterization of residual stresses from laser shock peening. Int. J. Fatigue 36, 96–108.

Cai, S., 2022. An iterative approach combined with multi-dimensional fitting of limited measured stress points to reconstruct residual stress field generated by laser shock peening. Surf. Coat. Technol. 19.

Cao, Z.w., Che, Z.g., Zou, S.k., Fei, Q.x., 2011. Numerical simulation of residual stress field induced by laser shock processing with square spot. J. Shanghai Jiaotong Univ. 15, 553–556, (English Edition).

Cellard, C., Osmond, P., Retraint, D., Rouhaud, E., Remy, S., Viguera-Sancho, A., 2007. Residual stress and deformation induced by laser shock peening on titanium alloys. In: Gdoutos, E.E. (Ed.), Experimental Analysis of Nano and Engineering Materials and Structures. Springer Netherlands, Dordrecht, pp. 69–70.

Cellard, C., Retraint, D., François, M., Rouhaud, E., Le Saunier, D., 2012. Laser shock peening of Ti-17 titanium alloy: Influence of process parameters. Mater. Sci. Eng. A 532, 362–372.

Chaieb, I., 2004. Analyse et simulation des contraintes résiduelles induites par des traitements mécaniques de précontrainte en grenaillage et choc laser (Ph.D. thesis). Université de Reims Champagne-Ardenne, Reims.

Clauer, A.H., 2019. Laser shock peening, the path to production. Metals 9 (626).

Cochennec, F., 2009. Simulation numérique du grenaillage de mise en forme pour une intégration produit-procédés en conception mécanique (Ph.D. thesis). Université de Technologie de Troyes.

Ding, K., 2003. Three-dimensional dynamic finite element analysis of multiple laser shock peening processes. Surface Engineering 19, 351–358.

Ding, K., Ye, L., 2006a. Laser Shock Peening Performance and Process Simulation. Woodhead Publishing Limited.

Ding, K., Ye, L., 2006b. Simulation of multiple laser shock peening of a 35CD4 steel alloy. J. Mater Process. Technol. 178, 162–169.

Ecault, R., Touchard, F., Boustie, M., Berthe, L., Dominguez, N., 2016. Numerical modeling of laser-induced shock experiments for the development of the adhesion test for bonded composite materials. Compos. Struct. 152, 382–394.

Fabbro, R., Fournier, J., Ballard, P., Devaux, D., Virmont, J., 1990. Physical study of laser-produced plasma in confined geometry. J. Appl. Phys. 68, 775–784.

Fox, J.A., 1974. Effect of water and paint coatings on laser-irradiated targets. Appl. Phys. Lett. 24, 461–464.

Gelineau, M., 2018. Etude de l'impact du grenaillage sur des composants mé (Ph.D. thesis). Ecole Nationale Supérieure des Arts et Métiers.

Gill, A.S., Telang, A., Vasudevan, V.K., 2015. Characteristics of surface layers formed on inconel 718 by laser shock peening with and without a protective coating. J. Mater Process. Technol. 225, 463–472.

Glaser, D., Polese, C., Venter, A., Marais, D., Plaisier, J., 2022. Evaluation of laser shock peening process parameters incorporating Almen strip deflections. Surf. Coat. Technol. 434, 128158.

Heuzé, T., 2017. Lax–Wendroff and TVD finite volume methods for unidimensional thermomechanical numerical simulations of impacts on elastic–plastic solids. J. Comput. Phys. 346, 369–388.

Hfaiedh, N., Peyre, P., Song, H., Popa, I., Ji, V., Vignal, V., 2015. Finite element analysis of laser shock peening of 2050-T8 aluminum alloy. Int. J. Fatigue 70, 480–489.

Hu, Y., Grandhi, R.V., 2012. Efficient numerical prediction of residual stress and deformation for large-scale laser shock processing using the eigenstrain methodology. Surf. Coat. Technol. 206, 3374–3385.

Johns, D.J., 1965. Thermal Stress Analyses. Pergamon press edition.

Johnson, G.R., Cook, W.H., 1983. A constitutive model ad data for metals subjected to large strains, high strain rates and high temperatures. Int. Ballist. Soc. 541–547.

Julan, E., 2014. Simulation numérique du choc laser pour la mise en compression en présence de l'état initial dû au soudage (Ph.D. thesis). Ecole Polytechnique.

Julan, E., Taheri, S., Stolz, C., Peyre, P., Gilles, P., 2014. Numerical simulation of laser shock peening in presence of weld for fatigue life. In: Design and Analysis. vol. 3, American Society of Mechanical Engineers, Anaheim, California, USA, p. V003T03A029.

Kim, J.H., Kim, Y.J., Lee, J.W., Yoo, S.H., 2014. Study on effect of time parameters of laser shock peening on residual stresses using FE simulation. J. Mech. Sci. Technol. 28, 1803–1810.

Korsunsky, A.M., 2005. The modelling of residual stresses due to surface peening using eigenstrain distributions. J. Strain Anal. Eng. Des. 40, 817–824.

Lapostolle, L., 2022. EVEREST. https://github.com/llapo/EVEREST.

Lapostolle, L., Derrien, K., Morin, L., Berthe, L., Castelnau, O., 2022. Modeling and simulation of laser shock waves in elasto-plastic 1D layered specimens. Int. J. Solids Struct. 239–240, 111422.

Le Bras, C., Rondepierre, A., Seddik, R., Scius-Bertrand, M., Rouchausse, Y., Videau, L., Fayolle, B., Gervais, M., Morin, L., Valadon, S., Ecault, R., Furfari, D., Berthe, L., 2019. Laser shock peening: Toward the use of pliable solid polymers for confinement. Metals 9 (793).

LeVeque, R.J., 1997. Wave propagation algorithms for multidimensional hyperbolic systems. J. Comput. Phys. 131, 327–353.

Leveque, R.J., 2002. Finite Volume Methods for Hyperbolic Problems. Cambridge university press edition.

Meyer, H.W., Kleponis, D.S., 2001. Modeling the high strain rate behavior of titanium undergoing ballistic impact and penetration. Int. J. Impact Eng. 26, 509–521.

Miao, H., Larose, S., Perron, C., Lévesque, M., 2010. An analytical approach to relate shot peening parameters to Almen intensity. Surf. Coat. Technol. 205, 2055–2066.

Milani, A., Dabboussi, W., Nemes, J., Abeyaratne, R., 2009. An improved multi-objective identification of Johnson–Cook material parameters. Int. J. Impact Eng. 36, 294–302.

Ming, L., Pantalé, O., 2018. An efficient and robust VUMAT implementation of elastoplastic constitutive laws in Abaqus/Explicit finite element code. Mech. Ind. 19 (308).

Montross, C., Wei, T., Ye, L., Clark, G., Mai, Y.W., 2002. Laser shock processing and its effects on microstructure and properties of metal alloys: a review. Int. J. Fatigue 24, 1021–1036.

Morin, L., Braham, C., Tajdary, P., Seddik, R., Gonzalez, G., 2021. Reconstruction of heterogeneous surface residual-stresses in metallic materials from X-ray diffraction measurements. Mech. Mater. 158, 103882.

Ocaña, J., Morales, M., Molpeceres, C., Torres, J., 2004. Numerical simulation of surface deformation and residual stresses fields in laser shock processing experiments. Appl. Surf. Sci. 238, 242–248.

Peyre, P., Berthe, L., Scherpereel, X., Fabbro, R., 1998. Laser-shock processing of aluminium-coated 55C1 steel in water-confinement regime, characterization and application to high-cycle fatigue behaviour. J. Mater. Sci. 142, 1–1429.

Peyre, P., Berthe, L., Vignal, V., Popa, I., Baudin, T., 2012. Analysis of laser shock waves and resulting surface deformations in an Al–Cu–Li aluminum alloy. J. Phys. D: Appl. Phys. 45, 335304.

Peyre, P., Chaieb, I., Braham, C., 2007. FEM calculation of residual stresses induced by laser shock processing in stainless steels. Modelling Simulation Mater. Sci. Eng. 15, 205–221.

Peyre, P., Fabbro, R., Merrien, P., Lieurade, H., 1996. Laser shock processing of aluminium alloys. Application to high cycle fatigue behaviour. Mater. Sci. Eng. A 210, 102–113.

Peyre, P., Sollier, A., Chaieb, I., Berthe, L., Bartnicki, E., Braham, C., Fabbro, R., 2003. FEM simulation of residual stresses induced by laser Peening. Eur. Phys. J. Appl. Phys. 23, 83–88.

Rondepierre, A., Rouchausse, Y., Videau, L., Casagrande, O., Castelnau, O., Berthe, L., 2021. Laser interaction in a water tank configuration: Higher confinement breakdown threshold and greater generated pressures for laser shock peening. J. Laser Appl. 33, 042022.

Rubio-González, C., Gomez-Rosas, G., Ocaña, J., Molpeceres, C., Banderas, A., Porro, J., Morales, M., 2006. Effect of an absorbent overlay on the residual stress field induced by laser shock processing on aluminum samples. Appl. Surf. Sci. 252, 6201–6205.

Scius-Bertrand, M., Videau, L., Rondepierre, A., Lescoute, E., Rouchausse, Y., Kaufman, J., Rostohar, D., Brajer, J., Berthe, L., 2021. Laser induced plasma characterization in direct and water confined regimes: new advances in experimental studies and numerical modelling. J. Phys. D: Appl. Phys. 54, 055204.

Seddik, R., Rondepierre, A., Prabhakaran, S., Morin, L., Favier, V., Palin-Luc, T., Berthe, L., 2022. Identification of constitutive equations at very high strain rates using shock wave produced by laser. Eur. J. Mech. A Solids 92, 104432.

Simo, J.C., Taylor, R.L., 1986. A return mapping algorithm for plane stress elastoplasticity. Internat. J. Numer. Methods Engrg. 22, 649–670.

Song, H., 2010. Analyse expérimentale et numérique de la distribution des contraintes résiduelles induites par choc-laser dans les alliages d'aluminium (Ph.D. thesis). Ecole Nationale Supérieure des Arts et Métiers.

Tada, H., Paris, P.C., 1983. The stress intensity factor for a crack perpendicular to the welding bead. Int. J. Fract. 21, 279–284.

Taddia, S., Troiani, E., 2015. Effect of laser shock peening on the fatigue behavior of thin aluminum panels. Mater. Today Proc. 2, 5006–5014.

Umbrello, D., M'Saoubi, R., Outeiro, J., 2007. The influence of Johnson–Cook material constants on finite element simulation of machining of AISI 316L steel. Int. J. Mach. Tools Manuf. 47, 462–470.

Zhang, D.N., Shangguan, Q.Q., Xie, C.J., Liu, F., 2015. A modified Johnson–Cook model of dynamic tensile behaviors for 7075-T6 aluminum alloy. J. Alloys Compd. 619, 186–194.